

FEATURE ARTICLE

Fundamental Properties of Single-Wall Carbon Nanotubes

Carter T. White^{*,†} and John W. Mintmire[‡]

Naval Research Laboratory, Washington, D.C. 20375-5320, and Department of Physics, Oklahoma State University, Stillwater, Oklahoma 74078-3072

Received: June 15, 2004; In Final Form: July 23, 2004

Single-wall carbon nanotubes (SWCNTs) represent an excellent example of materials by design with many of their outstanding properties predicted by theory prior to their synthesis. Both experimental and theoretical work on these novel nanowires continue to increase at a breathtaking pace. Herein we describe some of their fundamental properties on which much of this work is built. After discussing their structure and symmetries, we emphasize their exceptional electronic properties. The standard one-parameter graphene sheet model of SWCNTs, introduced in the earliest published paper on extended SWCNTs, is discussed in terms of both its successes and limitations. The strong interplay between theory and experiment that this area has enjoyed is also discussed. In addition, several opportunities for further study are touched upon.

Introduction

At the intersection of fullerenes,¹ carbon fibers,² and conducting polymers,³ single-wall carbon nanotubes (SWCNTs) represent a novel class of low-dimensional materials exhibiting exceptional electronic properties.^{4–13} Many of these properties were predicted by theory^{14–21} prior to the successful synthesis of SWCNTs.^{22–24} The synthesis of SWCNTs followed the large-scale production of multiwall carbon nanotubes²⁵ initially observed by Iijima²⁶ in carbon samples produced using a carbon-arc-discharge method for fullerene synthesis.²⁷ Multiwall carbon tubes were known in the earlier carbon fiber literature with diameters down to 10 nm.²

Herein, we provide a survey of some of the fundamental electronic and structural properties of SWCNTs with emphasis on their unique electronic properties. We start with a discussion of their structure and symmetries.¹⁹ We then discuss the metallic SWCNTs,^{4–6,11,14–17} touching upon their special electronic structure that allows these nanowires not only to effectively resist a spontaneous symmetry breaking that would convert them to semiconductors¹⁴ but also to support ballistic electron transport over large distances^{4,12,13} in the presence of disorder.^{28–30} Next, we discuss the small and large band gap semiconducting SWCNTs.^{5,6,11,15–20,31,32} We then discuss the standard graphene sheet model (GSM) for SWCNTs,^{14,16,17} pointing out its successes and limitations when compared to more sophisticated calculations.^{14–16,18,20} (A closely related approach to the standard GSM is the $\mathbf{k}\cdot\mathbf{p}$ scheme of Ando and co-workers from which many important results have been obtained.³³) Next, we discuss some of the key nanotube experimental results^{4–13,34,35} with emphasis on the strong interplay between theory^{14–20,28–30,36,37} and experiment^{4–13,22–25,34,35} that this area has enjoyed. We then

turn to some current fundamental issues awaiting resolution. Finally, we conclude with brief comments.

Structure And Symmetries Of Single-Wall Carbon Nanotubes

Structure from the Graphene Sheet. All extended SWCNTs can be visualized as a conformal mapping of 2D graphite (termed graphene) onto the surface of a cylinder.²⁶ Thus, the proper boundary conditions around the cylinder can only be satisfied if the circumference of the cylinder maps onto one of the Bravais lattice vectors of the graphene sheet as shown in Figure 1.^{15–17} In addition, each Bravais lattice vector, \mathbf{R} , can be defined in terms of the two primitive lattice vectors \mathbf{R}_1 , \mathbf{R}_2 for graphene depicted in Figure 1 and a pair of integers $[n_1, n_2]$ so that

$$\mathbf{R} = n_1\mathbf{R}_1 + n_2\mathbf{R}_2 \quad (1)$$

(Note that if the x axis in a right-hand coordinate system is oriented along \mathbf{R}_1 , then \mathbf{R}_1 and \mathbf{R}_2 are given by $\mathbf{R}_1 = a\mathbf{i}$ and $\mathbf{R}_2 = (a/2)\mathbf{i} + (a\sqrt{3}/2)\mathbf{j}$, where $a = \sqrt{3}d$ is the graphene lattice spacing with d the C–C bond distance, and \mathbf{i} and \mathbf{j} denote the usual unit vectors along the x and y axes, respectively.) Thus, all unrelaxed SWCNTs can be constructed by rolling up a single graphene sheet along one of its 2D lattice vectors \mathbf{R} given by eq 1 to define a $[n_1, n_2]$ nanotube with radius

$$r = \frac{|\mathbf{R}|}{2\pi} = \frac{a}{2\pi} \sqrt{n_1^2 + n_2^2 + n_1n_2} \quad (2)$$

The point-group symmetry of the graphene lattice will make many of the SWCNTs defined by \mathbf{R} equivalent. Indeed, this symmetry allows \mathbf{R} to be restricted to the irreducible wedge of the graphene lattice depicted in Figure 2, without loss of generality.^{15–17,38} Each \mathbf{R} within this wedge defines a different

* Corresponding author. E-mail: carter.white@nrl.navy.mil.

[†] Naval Research Laboratory.

[‡] Oklahoma State University.

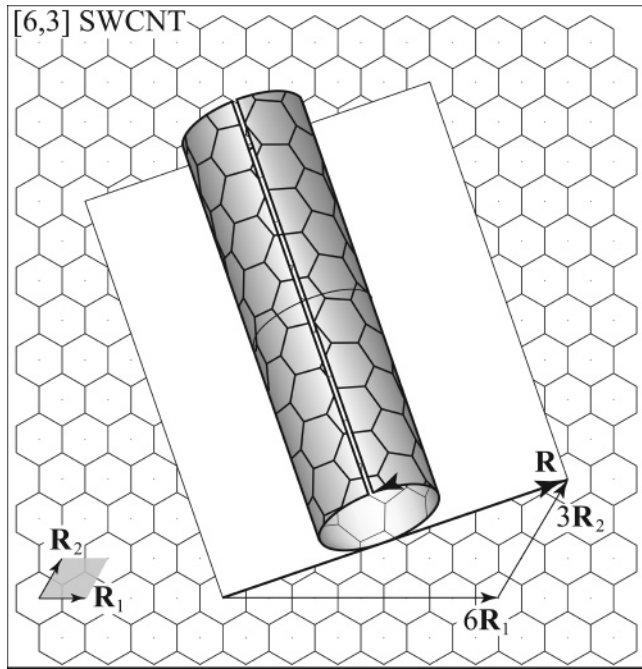


Figure 1. Mapping of the graphene sheet to form the [6,3] SWCNT with a couple of translational unit cells along the tube shown. The unit cell of the graphene lattice highlighted in gray is defined by the primitive lattice vectors \mathbf{R}_1 and \mathbf{R}_2 .

SWCNT, and all unique SWCNTs defined by rolling up the graphene sheet can be generated by this set of \mathbf{R} 's. Also, within this wedge only a finite number of SWCNTs can be constructed with radii below a given value. The angle, Θ , measured counterclockwise from \mathbf{R}_1 to the roll-up vector \mathbf{R} , is usually referred to as the chiral angle for the SWCNT. In terms of n_1 and n_2 , Θ is given by

$$\Theta = \arccos\left(\frac{\mathbf{R}_1 \cdot \mathbf{R}}{|\mathbf{R}_1||\mathbf{R}|}\right) = \arccos\left(\frac{2n_1 + n_2}{2\sqrt{n_1^2 + n_2^2 + n_1n_2}}\right) = \arctan\left(\frac{\sqrt{3}n_2}{2n_1 + n_2}\right) \quad (3)$$

for tubes defined in terms of the irreducible wedge of Figure 2. The set of possible tubes defined by \mathbf{R} can be completely decomposed into independent families (subsets) with each family member sharing the same orientation of hexagons with respect to the tube axis and hence the same Θ . Thus, rather than labeling the SWCNTs by $[n_1, n_2]$, they could just as well have been labeled by $N[q_1, q_2]$, where $[q_1, q_2]$ denotes the family to which $[n_1, n_2]$ belongs and N is the largest common divisor of $[n_1, n_2]$.¹⁶ Unless otherwise specified we will use the $[n_1, n_2]$ notation to label SWCNTs.

The construction of the tubule from a conformal mapping of the graphite sheet shows that each tubule can have up to three inequivalent (by point group symmetry) helical operations derived from the primitive lattice vectors of the graphite sheet. Thus, while *all* SWCNTs have a helical structure, the two families of tubules defined by rollup vectors with chiral angles $\Theta = 0$ or 30° in Figure 2 (which correspond to lattice translation indices of the form $[n, 0]$ and $[n, n]$, respectively) will possess a reflection plane. These high-symmetry SWCNTs will therefore be achiral. For convenience, these special structures are given family names based on the shapes made by the most direct

continuous path of C–C bonds around the circumference of the tubule. Specifically, the $[n, 0]$ -type structures are referred to as zigzag¹⁷ or sawtooth³⁸ tubes to reflect the path highlighted in gray for the $[9, 0]$ tube at the top of Figure 3, and the $[n, n]$ -type structures are referred to as armchair¹⁷ or serpentine³⁸ tubes to reflect the path highlighted in gray for the $[5, 5]$ tube at the bottom of Figure 3. For other values of Θ the tubules are chiral and have three inequivalent helical operations. The tube can be rolled up either above (as shown in Figure 1) or below the plane of the graphene sheet. These two tubes can be thought of as mirror images of one another, with the graphene sheet defining the mirror plane. For the achiral tubes this plane is also a reflection plane and the two tubes are identical. However, all other SWCNTs have a left or right-handedness, and hence the tube and its mirror image will be different. The tube properties discussed in this article do not depend on whether the tube is left or right-handed. However, any asymmetric perturbation that can distinguish handedness will be able to tell them apart.

Translational Symmetry. Regardless of whether they are chiral or achiral, all SWCNTs defined by \mathbf{R} in the graphene lattice have translational symmetry along the tube axis¹⁵ with a repeat length given by $\sqrt{3}|\mathbf{R}|$, as can be seen by inscribing a hexagon with a side coinciding with \mathbf{R} in the lattice prior to rolling up the sheet. An example is given in Figure 4 for the $[4, 2]$ tube. It might happen that $\sqrt{3}|\mathbf{R}|$ is not the minimum translational repeat length. Indeed, by constructing a vector, $\mathbf{T} = -(2n_2 + n_1)\mathbf{R}_1 + (2n_1 + n_2)\mathbf{R}_2$ perpendicular to \mathbf{R} but lying in the honeycomb lattice, it is immediately seen that the minimum translational repeat length is given by $\sqrt{3}|\mathbf{R}|/L$ where L is the largest common divisor of $(2n_2 + n_1)$ and $(2n_1 + n_2)$. Hence, $L = N$, unless there exists an integer m such that $(n_1 - n_2)/N = 3m$, in which case $L = 3N$.¹⁹

Although, all SWCNTs defined by rolling up the graphene sheet have translational symmetry, the minimum number of atoms in a translational unit cell can be large.¹⁹ To see this, first note that the unit cell in graphene contains two atoms and has area given by $A_g = |\mathbf{R}_1 \times \mathbf{R}_2| = \sqrt{3}a^2/2$. Next, note that the area of the strip that is rolled up to form the minimum sized translational unit cell of the tube is given by: $A_T = \sqrt{3}|\mathbf{R}|^2/L = \sqrt{3}a^2(n_1^2 + n_2^2 + n_1n_2)/L$. Hence, the translational unit cell of the SWCNT contains N_A carbon atoms given by

$$N_A = 2 \frac{A_T}{A_g} = 4 \frac{(n_1^2 + n_2^2 + n_1n_2)}{L} \quad (4)$$

where

$$L = \begin{cases} 3N & \text{if } (n_1 - n_2)/N = 3m, \text{ with } m \text{ an integer} \\ N & \text{otherwise} \end{cases} \quad (5)$$

and N is the largest common divisor of n_1 and n_2 . For both the armchair $[n, n]$ and zigzag $[n, 0]$ tubes, eqs 4 and 5 imply that $N_A = 4n$, greatly reducing the number of atoms in the minimum translational unit cell. In these two special cases eqs 2 and 4 show that N_A scales as the radius, r , of the tube. It is for this reason that calculations relying on translational symmetry are usually restricted to these two special families of SWCNTs.^{16,17} On the other hand, L is often 1 so that N_A scales as r^2 , leading to a large number of atoms in the translational unit cell even for moderate diameter SWCNTs. For example, if $n_1 = 10$ and $n_2 = 9$, then the radius of the nanotube is less than 0.7 nm, but from eq 4 the translational unit cell contains 1084 carbon atoms. The rapid growth in the number of atoms that can occur in the minimum translational unit cell makes recourse to the helical

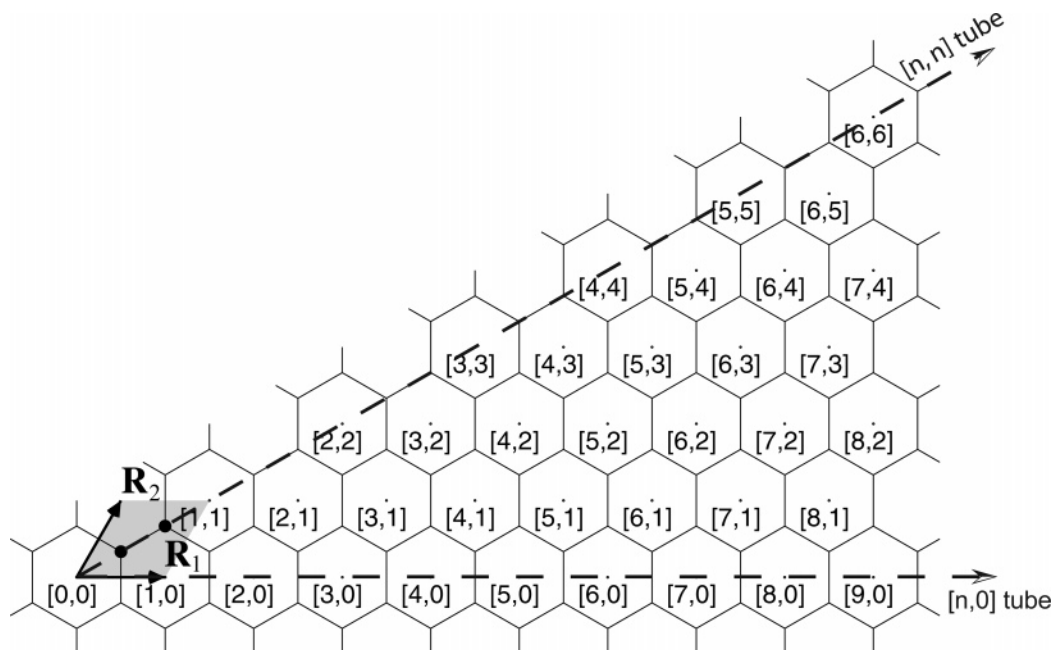


Figure 2. Irreducible wedge of the graphene lattice. Primitive lattice vectors \mathbf{R}_1 and \mathbf{R}_2 are shown and the [0,0] unit cell at the origin highlighted in gray. Armchair (serpentine) nanotubes are defined by rollup vectors \mathbf{R} along the $[n,n]$ direction corresponding to a chiral angle of $\pi/6$. Zigzag (sawtooth) SWCNTs are defined by rollup vectors \mathbf{R} along the $[n,0]$ direction corresponding to chiral angle of 0.

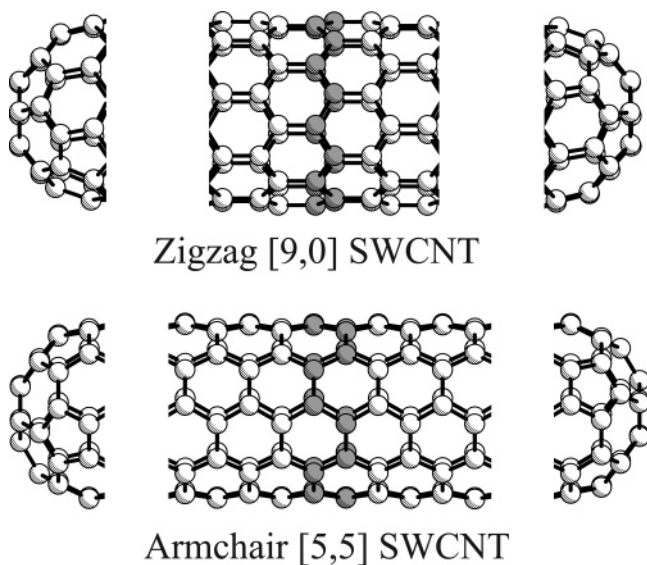


Figure 3. Sample achiral zigzag (sawtooth) and armchair (serpentine) SWCNTs. Highlighted in gray is the most direct continuous path along C–C bonds around the tube. The shape of this path gives these structures their family names. These two examples can be capped with a hemisphere of C_{60} .

and any higher point group symmetry of these nanotubes practically mandatory in any comprehensive study of their properties as a function of radius and helicity. As we shall see below, these symmetries can be used to reduce to 2 the number of atoms necessary to generate any nanotube.¹⁹

Helical and Rotational Symmetries. The rotational and helical symmetries of a SWCNT defined by \mathbf{R} can be seen by using the corresponding symmetry operators to generate the tubule.¹⁹ This is done by first introducing a cylinder of radius $|\mathbf{R}|/2\pi$. The two carbon atoms located at $\mathbf{d} \equiv (\mathbf{R}_1 + \mathbf{R}_2)/3$ and $2\mathbf{d}$ in the [0,0] unit cell of Figure 2 are then mapped to the surface of this cylinder. The first atom is mapped to an arbitrary point on the cylinder surface, which requires that the position

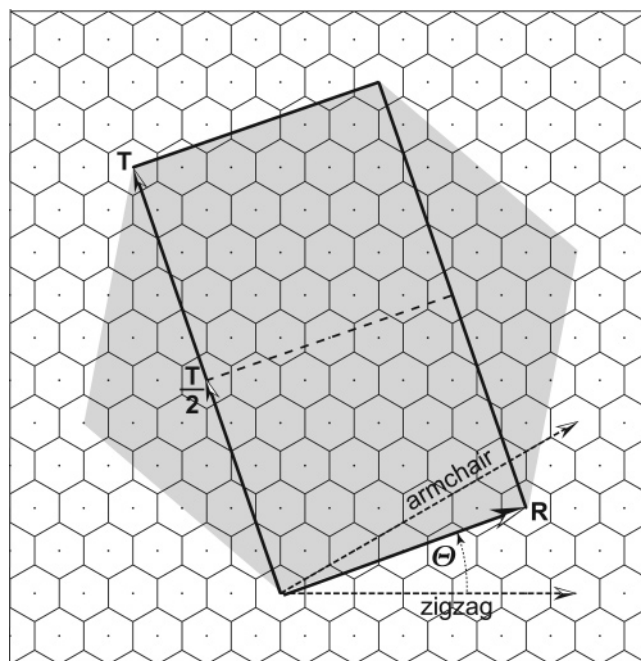


Figure 4. Rollup vector \mathbf{R} , translation vector \mathbf{T} , and chiral angle Θ for the [4,2] SWCNT. The hexagon highlighted in gray shows that this tube has translational symmetry along the tube axis. For the [4,2], L is 2, hence the minimum translational repeat length is given by $|\mathbf{T}|/2$, which from the properties of the hexagon equals $\sqrt{3}|\mathbf{R}|/2$.

of the second be found by rotating this point by

$$\phi' = 2\pi \frac{\mathbf{d} \cdot \mathbf{R}}{|\mathbf{R}|^2} = \frac{(n_1 + n_2)}{(n_1^2 + n_2^2 + n_1 n_2)} \pi \quad (6)$$

about the cylinder axis in conjunction with a translation

$$h' = \frac{|\mathbf{d} \times \mathbf{R}|}{|\mathbf{R}|} = \frac{(n_1 - n_2)}{2\sqrt{3}(n_1^2 + n_2^2 + n_1 n_2)^{1/2}} a \quad (7)$$

along this axis. Next, note that the cylinder axis must coincide with a C_N rotational axis for the tubule, where N is the largest common divisor of n_1 and n_2 . Thus, the positions of these first two atoms can be used to locate $2(N-1)$ additional atoms on the cylinder surface by $(N-1)$ successive $2\pi/N$ rotations about the cylinder axis. Altogether, these $2N$ atoms complete the specification of the helical motif that corresponds to an area on the cylinder surface given by $A_M = N|\mathbf{R}_1 \times \mathbf{R}_2| = (\sqrt{3}/2)Na^2$. This helical motif can then be used to tile the remainder of the tubule by repeated application of a single screw operation $S(h, \phi)$ representing a translation h units along the cylinder axis in conjunction with a rotation ϕ radians about this axis.

To find h and ϕ and hence determine $S(h, \phi)$, first note that there must exist a real lattice vector

$$\mathbf{H} = p_1 \mathbf{R}_1 + p_2 \mathbf{R}_2 \quad (8)$$

in the honeycomb lattice that maps to $S(h, \phi)$ when the sheet is rolled up along \mathbf{R} to form the tube. In terms of \mathbf{H} and \mathbf{R} , the area of the helical motif on the cylinder surface, A_M , equals $|\mathbf{H} \times \mathbf{R}|$. However, A_M also equals $N|\mathbf{R}_1 \times \mathbf{R}_2|$. Therefore, $|\mathbf{H} \times \mathbf{R}| = N|\mathbf{R}_1 \times \mathbf{R}_2|$, or equivalently,¹⁹

$$p_2 n_1 - p_1 n_2 = \pm N \quad (9)$$

There are no other constraints on \mathbf{H} and hence on $S(h, \phi)$. If a set of integers $\{p_1, p_2\}$ satisfies eq 9, then so too will the sets $\{p_1 \pm mn_1, p_2 \pm mn_2 | m \in \text{integers}\}$ and $\{-p_1, -p_2\}$. These uncertainties arise because ϕ is defined modulo 2π and if $S(h, \phi)$ generates the tubule, then so will $S(-h, -\phi)$. Typically, \mathbf{R} is restricted to the irreducible wedge of Figure 2 ($n_1 \geq n_2 \geq 0$), p_1 taken so that $p_1 \geq 0$, the plus sign is chosen in eq 9, and then the solution set which yields a minimum value of $|\mathbf{H} \cdot \mathbf{R}|$ found. These choices restrict $S(h, \phi)$ to a right-handed screw operation along the positive tubule axis that yields a minimum twist angle ϕ around this axis. In contrast to the helical twist angle given by

$$\phi = 2\pi \frac{\mathbf{H} \cdot \mathbf{R}}{|\mathbf{R}|^2} = \frac{(2p_1 + p_2)n_1 + (2p_2 + p_1)n_2}{(n_1^2 + n_2^2 + n_1 n_2)} \pi \quad (10)$$

the magnitude of helical translation given by

$$|h| = \frac{|\mathbf{H} \times \mathbf{R}|}{|\mathbf{R}|} = \frac{N|\mathbf{R}_1 \times \mathbf{R}_2|}{|\mathbf{R}|} = \frac{\sqrt{3}Na}{2\sqrt{n_1^2 + n_2^2 + n_1 n_2}} \quad (11)$$

is independent of the choice of \mathbf{H} . These results show that every tubule defined by \mathbf{R} can be generated by first mapping only two atoms onto the surface of a cylinder of radius $|\mathbf{R}|/2\pi$ and then using the rotational and helical symmetry operators to determine the remainder of the tubule.

As an example,¹⁹ consider the [6,3] tubule shown in Figure 1 defined by $\mathbf{R} = 6\mathbf{R}_1 + 3\mathbf{R}_2$. Then from eqs 2, 6, and 7, the first atom of this tubule is mapped to an arbitrary point on the surface of a cylinder of radius $3a\sqrt{7}/2\pi$ and the position of the second is then found by rotating this point $\pi/7$ radians around the cylinder axis in conjunction with a translation $a/(2\sqrt{21})$ units along this axis. Because N equals 3, the cylinder axis must coincide with a C_3 axis for the tubule. Thus, the positions of these first two atoms can be used to locate four additional atoms on the cylinder surface by two successive $2\pi/3$ rotations around this axis. Altogether, these six atoms complete the specification of the helical motif for this tubule. To determine $S(h, \phi)$ used to generate the remainder of the tubule from this motif, eq 9 can

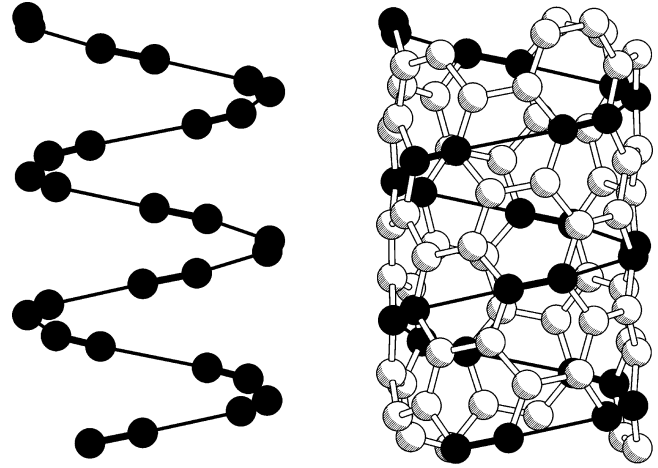


Figure 5. Left: One-third of the [6,3] tubule generated by applying $S(h, \phi)$ with $\phi = 3\pi/7$ and $h = a\sqrt{3}/(2\sqrt{7})$ to only the first two atoms mapped to the cylinder. Thin dark lines are not bonds but are rather included as a guide to the eye. Right: This same one-third plus the remaining two-thirds of the [6,3] tubule generated by applying $S(h, \phi)$ to the full six-atom helical motif. (Reprinted from ref 19.)

be solved subject to the constraints above to find the solution set $\{1, 1\}$. Hence, $\mathbf{H} = \mathbf{R}_1 + \mathbf{R}_2$, which in turn using eqs 10 and 11 implies that $\phi = 3\pi/7$ and $h = a\sqrt{3}/(2\sqrt{7})$. If this resultant $S(h, \phi)$ is applied to only the first two atoms mapped to the cylinder surface, then one-third of the tubule is generated as illustrated at the left of Figure 5. However, if the full helical motif is used, then the entire structure is generated as shown at the right of Figure 5.

Actual SWCNTs should relax somewhat from the geometry expected from rolling up a graphene sheet. However, first-principles LDF calculations have shown that the geometry predicted by rolling up the graphene sheet is quite close to the actual optimized tube geometry for SWCNTs that are typically studied experimentally.²⁰

Use of Helical and Rotational Symmetries. The helical and rotational symmetries of SWCNTs are broadly useful in studies of their properties. For example, they can reduce the size of the matrices that have to be diagonalized in a calculation of the nanotube's electronic structure to one no larger than that encountered in a corresponding electronic structure calculation of two-dimensional graphite.¹⁹ To see how this is done, first assume that each carbon atom in a tubule is described by j atomic-centered basis functions. Next, let (m, l) denote a cell in the tubule generated by first mapping the [0,0] unit cell of Figure 1 to the surface of the cylinder and then translating and rotating this cell by l applications of the rotational operator C_N followed by m applications of $S(h, \phi)$. Like the helical motif, these cells tile the tubule, but contain 2 instead of $2N$ carbon atoms. Now let $|m, l\rangle$ denote the $2j$ basis functions centered on the two carbon atoms contained in the tubule cell labeled by (m, l) . Then, because $S(h, \phi)$ and C_N commute, symmetry adapted generalized Bloch sums given by

$$|\kappa, n\rangle = \lim_{M \rightarrow \infty} \frac{1}{\sqrt{2NM}} \sum_{m=-M}^{M-1} \sum_{l=0}^{N-1} e^{-i\kappa m} e^{-2\pi i n l / N} |m, l\rangle \quad (12)$$

can be constructed such that

$$C_N |\kappa, n\rangle = e^{2\pi i n / N} |\kappa, n\rangle \quad \text{with} \quad n = 0, \dots, N-1 \quad (13)$$

and

$$S(h, \phi)|\kappa, n\rangle = e^{i\kappa}|\kappa, n\rangle \quad \text{with} \quad -\pi \leq \kappa < \pi \quad (14)$$

Just as \mathbf{H} maps to $S(h, \phi)$ when graphene is rolled up along \mathbf{R} to form the tube, the scalar product $\mathbf{k} \cdot \mathbf{H}$ maps to κ of the tube, where $\hbar\mathbf{k}$ is the usual 2D crystalline momentum of the sheet, i.e.,

$$\kappa = \mathbf{k} \cdot \mathbf{H} \quad (15)$$

Next, note that the matrix elements of the Hamiltonian, \mathcal{H} , between these generalized Bloch functions must vanish due to symmetry, unless $n = n'$ and $\kappa = \kappa'$ so that

$$\langle \kappa', n' | \mathcal{H} | \kappa, n \rangle = \delta_{nn'} \delta_{\kappa\kappa'} \sum_{m=-\infty}^{\infty} \sum_{l=0}^{N-1} e^{-i\kappa m} e^{-2\pi i n l / N} \langle 0, 0 | \mathcal{H} | m, l \rangle \quad (16)$$

Thus, eq 16 reduces the matrices to be diagonalized in a tubule band structure calculation to a size no larger than those encountered in a corresponding band structure calculation for graphene. For example, if we assume an all-valence carbon s and p tight-binding model with four states per atom, then the problem is reduced to the diagonalization of a 8×8 matrix for each κ and n .

Electronic Structure Of Single-Wall Carbon Nanotubes

Graphene and Graphite. To prepare to discuss the electronic properties of SWCNTs, first consider the band structure of graphene.^{39,40} The carbon atoms forming the honeycomb lattice of graphene each have three nearest neighbors and four valence electrons. Three of these valence electrons are tied up in sp^2 σ bonds with neighboring carbon atoms with the fourth contributing to the π bands of the material; σ bonds are typically stronger than π bonds and hence the bonding σ bands are totally occupied. The π bands are made up of $|p_z\rangle$ orbitals oriented normal to the graphene sheet with each carbon atom in the lattice contributing one spin degenerate orbital centered on that atom. Because the graphene sheet coincides with the nodal plane for these π orbitals, the π bands of graphene (formed from the interaction between these orbitals) separate by symmetry from the σ bands. Furthermore, because there is only one electron per spin degenerate orbital, the Fermi level, ϵ_F , must lie somewhere within the region of π bands. Hence, it is these bands that are of interest in determining the electronic properties of the material.

The π bands of graphene can be analyzed using a simple tight-binding Hamiltonian characterized by a single Slater–Koster parameter, $V_{pp\pi} \approx -2.7$ to -3 eV, the hopping matrix element between $|p_z\rangle$ orbitals associated with nearest neighboring C–C atoms in the graphene sheet. Introducing the usual Bloch sums of $|p_z\rangle$ orbitals, this Hamiltonian reduces to a 2×2 matrix that is readily diagonalized to yield the one-electron dispersion relations

$$\epsilon_{\pm}(\mathbf{k}) = \epsilon_F \pm |V_{pp\pi}| \sqrt{3 + 2 \cos \mathbf{k} \cdot \mathbf{R}_1 + 2 \cos \mathbf{k} \cdot \mathbf{R}_2 + 2 \cos \mathbf{k} \cdot (\mathbf{R}_1 - \mathbf{R}_2)} \quad (17)$$

in terms of the 2D crystalline momentum $\hbar\mathbf{k}$ and the primitive lattice vectors \mathbf{R}_1 and \mathbf{R}_2 . Next consider the standard reciprocal lattice vectors \mathbf{K}_1 and \mathbf{K}_2 for the graphene lattice given by $\mathbf{K}_i \cdot \mathbf{R}_j = 2\pi\delta_{ij}$, so that $\mathbf{K}_1 = (2\pi/a)\mathbf{i} - (2\pi/\sqrt{3}a)\mathbf{j}$ and $\mathbf{K}_2 = (4\pi/\sqrt{3}a)\mathbf{j}$. The band structure can then be restricted to a

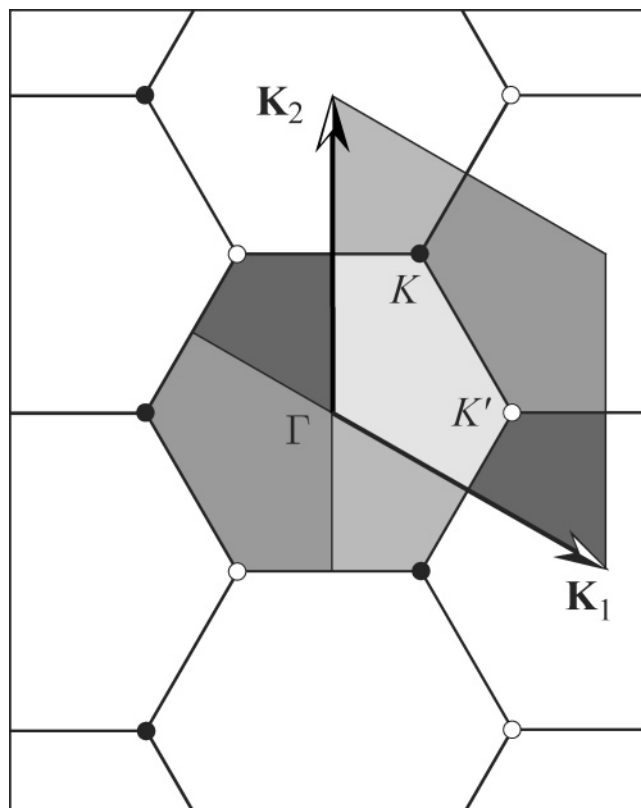


Figure 6. Graphene reciprocal lattice defined by the primitive reciprocal lattice vectors \mathbf{K}_1 and \mathbf{K}_2 . The central hexagonal Brillouin zone is depicted in several shades of gray to indicate regions related by reciprocal lattice vectors to corresponding regions of the primitive unit cell defined by \mathbf{K}_1 and \mathbf{K}_2 . Two of the high-symmetry inequivalent K points (under translational symmetry) at the corners of the hexagonal zone are labeled as K and K' , and these, as well as equivalent points in the lattice, are shown as black and white circles, respectively.

hexagonal unit cell (central Brillouin zone) of the reciprocal lattice because the dispersion relations must be periodic from unit cell to unit cell of the reciprocal lattice. The relationship of the central Brillouin zone of graphene to the unit cell of the reciprocal lattice defined by \mathbf{K}_1 and \mathbf{K}_2 is shown in Figure 6. Several high symmetry points of the central Brillouin zone are also labeled in Figure 6.

Of special interest are the K points at the six corners of the hexagonal zone because states with these wave vectors lie at ϵ_F .^{39,40} More specifically, the band structure given by eq 17 will have a band crossing (i.e., the occupied band and the unoccupied band will touch at ϵ_F) at the six corners K of the hexagonal Brillouin zone, as shown in Figure 7. The Fermi level is pinned at this crossing. The allowed degeneracies at the K points are a consequence of the translational symmetry of the honeycomb lattice and hence not a result of the approximations used to arrive at the one-parameter tight-binding model. Thus, this degeneracy will persist if overlap and longer range interactions are included in the model.³⁹ It will also persist in more complex first-principles LDF calculations.⁴⁰

These six corners of the central Brillouin zone are given by the vectors: $\mathbf{k}_F \equiv \pm(\mathbf{K}_1 - \mathbf{K}_2)/3$; $\pm(2\mathbf{K}_1 + \mathbf{K}_2)/3$; and $\pm(\mathbf{K}_1 + 2\mathbf{K}_2)/3$. However, only two of these points (labeled K and K' and shown as shaded and open circles in Figures 6 and 7) are inequivalent, yielding four spin degenerate states at ϵ_F . The remaining four points at the corners of the hexagonal zone are related to these two points by reciprocal lattice vectors and hence properly assigned to neighboring hexagons.

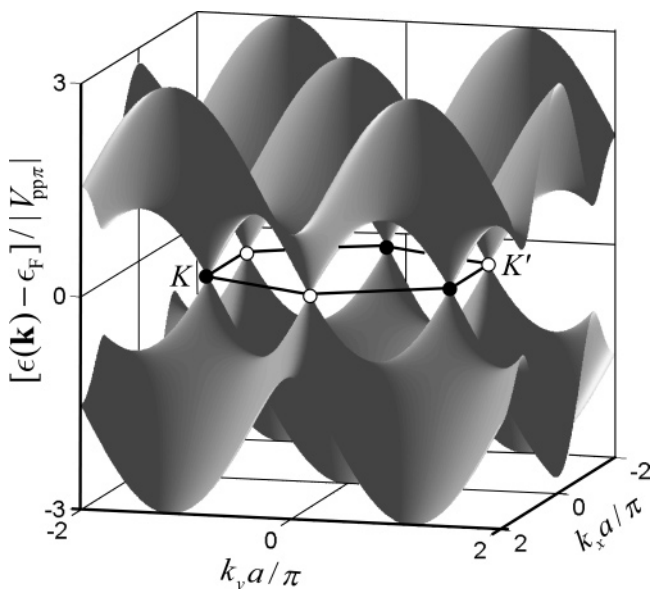


Figure 7. Dispersion relations of graphene from the one parameter tight-binding model over the central hexagonal Brillouin zone of the 2D reciprocal lattice of graphene with two of the inequivalent (under translational symmetry) high-symmetry K points at the corners of the zone labeled as K and K' .

The energy dispersion relations $\epsilon_{\pm}(\mathbf{k})$ given by eqs 17 have cusps at K and K' , but $\epsilon_{\pm}^2(\mathbf{k})$ is well behaved and can be expanded in a Taylor series in terms of $\Delta k \equiv |\mathbf{k} - \mathbf{k}_F|$ to get^{20,39}

$$\epsilon_{\pm}(\mathbf{k}) = \epsilon_F \pm \frac{\sqrt{3}}{2} |V_{pp\pi}| a |\mathbf{k} - \mathbf{k}_F| \quad (18)$$

valid to first order in $a|\mathbf{k} - \mathbf{k}_F|$. The electronic density of states (DOS) per carbon atom of graphene in the vicinity of ϵ_F is then given by

$$\rho(E) = \frac{2|E - \epsilon_F|}{\sqrt{3}\pi V_{pp\pi}^2} \quad (19)$$

where the spin degeneracy and the two inequivalent Brillouin zone corners have been included in using eq 18 to obtain this result. The conductivity of a metal is typically modeled as a product of the carrier density and the carrier mobility, with the carrier density proportional to the DOS at ϵ_F , $\rho(\epsilon_F)$. Thus, although carriers in graphene should have a high mobility associated with a large $|V_{pp\pi}|$, the density of carriers at ϵ_F is zero. For 3D graphite formed by ABAB stacking of the graphene layers, the DOS of states at ϵ_F will be small but nonzero, arising from interlayer interactions. This small DOS leads to a correspondingly small carrier density, of the order of 10^{18} carriers/cm³ compared to the typical metal carrier densities of 10^{22} to 10^{23} carriers/cm³.

Metallic Carbon Nanotubes. Concurrent with the initial observation of multiwall carbon nanotubes, theorists independently predicted that armchair SWCNTs, if synthesized, should be metallic.¹⁴ They also predicted that these tubes would be stable to low temperatures against a spontaneous symmetry breaking that would convert them to semiconductors while having high carrier mobilities at ϵ_F , thus making them outstanding candidates for the ultimate metallic nanowires.¹⁴ More specifically it was predicted that armchair tubules with diameters around a nanometer are rigid enough to avoid a Peierls distortion to far below room temperature, which turns other potentially metallic 1D polymers such as polyacetylene into semiconduc-

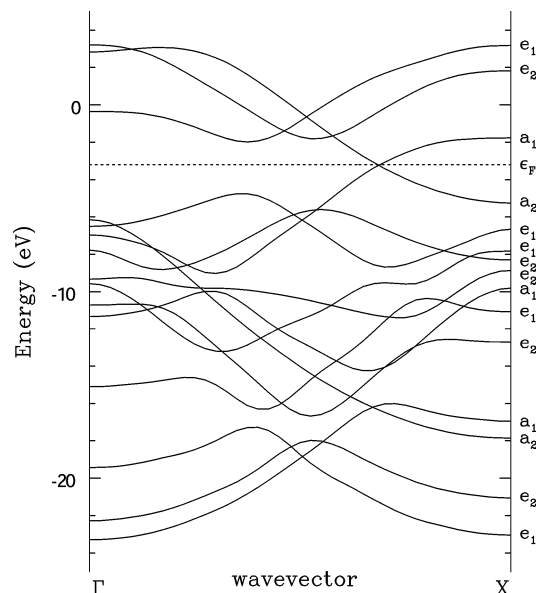


Figure 8. First-principles LDF band structures of [5,5] SWCNT as a function of the helical phase factor κ from 0 to π . The bands at $-\kappa$ are the same as those at κ . Hence results are plotted over only half of the central 1D zone. (Reprinted from ref 14.)

tors, while enjoying a high mobility comparable to the intraplanar mobility of pure graphite, without the very low DOS near ϵ_F that makes graphite a poor conductor. This remarkable combination of properties helped stimulate worldwide efforts first to synthesize these tubes^{22–25} and then measure their properties, resulting over five years later in the first direct experimental confirmation that these tubes were indeed metallic with outstanding transport properties.⁴

The initial theoretical work focused on the electronic structure of the $[n,n]$ armchair SWCNTs with special emphasis on the [5,5] tubule.¹⁴ This tubule can be capped by a hemisphere of C_{60} oriented along a 5-fold axis as depicted at the bottom of Figure 3. First-principles calculations were implemented using an all-electron, self-consistent local-density functional (LDF) band-structure method originally developed to treat chain polymers⁴¹ and especially tailored to take advantage of helical symmetry.⁴² Thus, the one-electron wave functions were constructed from linear combinations of these helically adapted Bloch functions, which in turn were constructed from linear combinations of atomic centered products of Gaussians and real solid spherical harmonics, and then these wave functions were used in solving the self-consistent LDF equations. The companion tight-binding studies also used the helical and rotational symmetries of the armchair tubes.

It was found that all armchair tubules are metals with two bands of different symmetry crossing approximately at $\kappa_F \approx \pm 2\pi/3$, with ϵ_F pinned to this crossing. These features are illustrated by the first-principles LDF band-structure results for the [5,5] tubule shown in Figure 8, where the a_1 and a_2 bands (obtained using a 7s3p Gaussian basis set and labeled by the irreducible representation of the C_{5v} point group) cross at $\kappa \approx \pm 0.69\pi$. It was also shown that armchair SWCNTs have a linear dispersion relation in the vicinity of ϵ_F given approximately by

$$\epsilon_{\pm}(\kappa) = \epsilon_F \pm \sqrt{3} |V_{pp\pi}| |\kappa - \kappa_F| \quad (20)$$

and this result was then used in establishing that those tubes with diameters approximately equal to or greater than the diameter of $I_h C_{60}$ should be stable against a spontaneous symmetry breaking.¹⁴ Note that, using $\kappa = ka/2$, appropriate

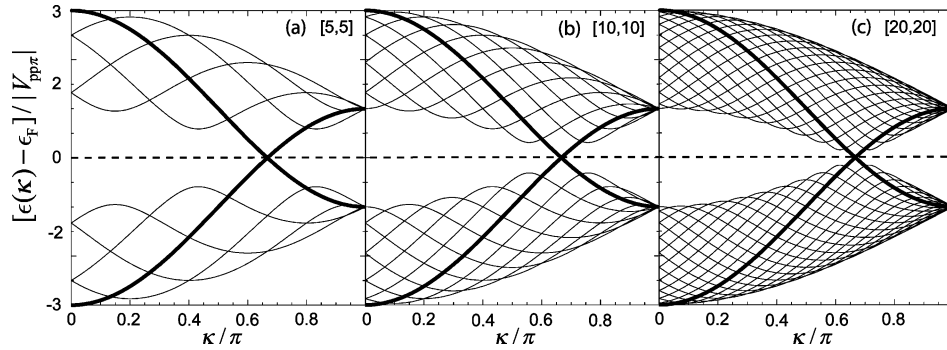


Figure 9. Band structures of a: [5,5], b: [10,10], and c: [20,20] SWCNTs from the standard GSM obtained by assuming that $\phi = \pi/5$, $\phi = \pi/10$, and $\phi = \pi/20$, respectively. The bands are drawn as a function of the helical phase factor κ from 0 to π . The invariant bands that cross at ϵ_F are depicted as heavy black lines. The bands at $-\kappa$ are the same as those at κ . Hence, results are plotted over only half of the central 1D zone.

for the bands that cross at ϵ_F , where $\hbar k$ is the usual crystalline momentum along the tube, eq 20 can be immediately recast as

$$\epsilon_{\pm}(k) - \epsilon_F = \pm \frac{\sqrt{3}|V_{pp\pi}|a}{2}|k - k_F| = \pm \hbar|\nu_F||k - k_F| \quad (21)$$

where

$$|\nu_F| = \frac{1}{\hbar} \left| \frac{d\epsilon(k)}{dk} \right|_{k=k_F} = \frac{\sqrt{3}|V_{pp\pi}|a}{2\hbar} \quad (22)$$

is the magnitude of the Fermi velocity and k_F (brought to within the central 1D Brillouin zone defined by the primitive translational unit cell of armchair tubes, $-\pi/a \leq k < \pi/a$, by adding or subtracting a primitive reciprocal lattice vector of magnitude, $2\pi/a$) is given by $k_F = \pm 2\pi/3a$. Hence, for an armchair SWCNT of radius r , the electronic density of states (DOS) per carbon atom in the vicinity of ϵ_F varies as $1/r$ (ref 14) and is given by

$$\rho(E) = \frac{1}{\pi^2|V_{pp\pi}|} \left(\frac{a}{r} \right) \quad (23)$$

where the spin degeneracy and equal contributions to the DOS at $\pm k$ have been included in using eq 21 to obtain this result. Thus, the small diameters of armchair nanotubes should allow them to enjoy a high carrier mobility comparable to the intraplanar mobility of pure graphite, without the very low DOS at ϵ_F that makes graphite a poor conductor.¹⁴

This outstanding combination of properties, however, is not sufficient to guarantee that armchair nanotubes are good metals.¹⁴ Indeed, Peierls pointed out long ago that any 1D metal would spontaneously break its initial symmetry to form a semiconductor.⁴³ This occurs because the 1D nature of the system demands that accompanying the distortion induced HOMO–LUMO gap are new divergences in the DOS at the gap edges. These divergences—peculiar to one dimension—in turn yield an energy lowering that always overcomes the elastic term resisting the distortion. Thus, for low enough temperatures the Peierls distortion cannot be prevented within a mean-field approach. However, it can be avoided if a system could be found where the density of electrons at ϵ_F is only sufficient to stabilize the broken symmetry state at very low temperatures but where this same density is still high enough to maintain a good metal. This combination of properties is exceptionally difficult to obtain. Nevertheless, it was exactly what was anticipated for armchair SWCNTs, with diameters as small as the [5,5].¹⁴

Armchair SWCNTs are able to resist a spontaneous symmetry breaking while still having a significant carrier density because of their remarkable electronic structure which is independent

of the tube's diameter near ϵ_F ,¹⁴ as shown in Figure 9. Thus, for larger and larger radius tubes the number of electrons driving the distortion remains constant while the elastic restoring force resisting it continues to increase—exponentially suppressing the temperature, $T_C \sim \exp(-Br)$, at which the symmetry breaking is stable, while the DOS only decreases as $1/r$.¹⁴

The invariance of the electronic structure of armchair tubes near ϵ_F also has important consequences for their transport properties in the presence of residual disorder.²⁸ Among the various probable sources of residual disorder (including bends caused by nanometer scale substrate features^{28,32} and long-range disorder arising from substrate charges²⁹), potential fluctuations varying of a scale of the C–C bond distance are probably the most effective in limiting the mean free path, l , for elastic electron backscattering along the tube.²⁸ However, electrons traveling along the nanotube do not directly experience the effects of such short-range disorder but rather its smoothed average over the tube's circumference. This causes l to increase linearly as larger and larger diameter tubes are considered.²⁸ There are practical limits, but this relationship between l and diameter means that residually disordered metallic tubes with nanometer diameters are probably able to sustain ballistic transport over micrometers when their chemical and mechanical stability and strong C–C interactions are taken into account.²⁸

The increase in l due to better averaging of the disorder in larger diameter tubes is possible only because of the diameter independent number of quantum states available for electron conduction through the tube. This key property of metallic SWCNTs allows conduction electrons in larger and larger diameter tubes to take progressively better advantage of averaging over the tube's circumference without having to confront additional states for electron backscattering.²⁸ Such additional states would appear in normal metallic wires with increasing transverse size, eliminating the benefits of disorder averaging and making l independent of the wire's transverse size. Thus, we see that the same remarkable property that makes armchair nanotubes stable against the Peierls distortion and hence metallic in the first place also plays a key role in enhancing their ballistic transport properties in the presence of residual disorder. This same property will also suppress the effects of acoustic phonon scattering just as it suppresses the Peierls distortion.

Also, note that small band gap SWCNTs (nanotubes that are not quite metallic because of their intrinsic structure to be discussed below) have an electronic structure near ϵ_F that is effectively independent of the tube's diameter insofar as the above analysis is concerned. Thus, if ϵ_F is slightly displaced from the small curvature induced gap in quasi-metallic SWCNTs, then they too should be metallic and stable against a Peierls

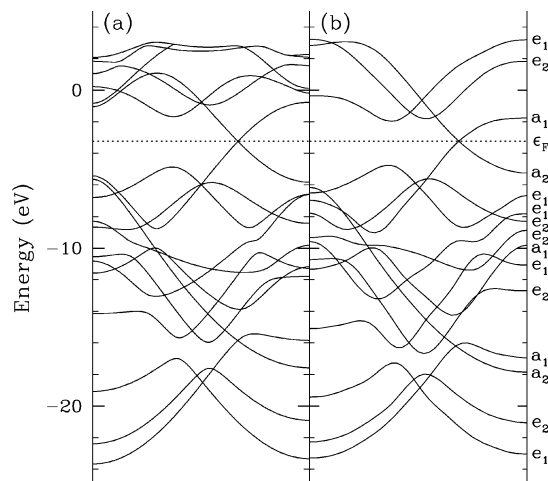


Figure 10. (a) Slater–Koster valence tight-binding and (b) first-principles LDF band structures of [5,5] SWCNT as a function of the helical phase factor κ from 0 to π . The Slater–Koster ϵ_F has been aligned with the calculated LDF ϵ_F . Results are plotted over only half of the central 1D zone. (Reprinted from ref 45.)

distortion to far below room temperature as well as exhibit exceptional ballistic transport properties, as has been observed.^{12,13,30} Finally, note that multiwall carbon nanotubes also exhibit exceptional ballistic transport properties.⁴⁴ In this case transport along the individual metallic tubes embedded in the multiwall tube will be perturbed by neighboring concentric tubes. These neighboring tubes, however, are likely to have different chiralities which could produce near random perturbations that fluctuate on a scale that is small with respect to the nanotube diameter. Hence, averaging over the tube's circumference leading to enhanced ballistic transport for larger and larger diameter tubes could again occur so long as the intertube interactions do not affect the number of channels for conduction along the metallic tube. In this context it is noteworthy that much larger diameter tubes can be supported in a multiwall geometry; in an isolated geometry, if their diameter is too large, they collapse.

Semiconducting Carbon Nanotubes. Helical and rotational symmetries were also used in the first band structure calculations of extended chiral SWCNTs defined through the conformal mapping from the graphite sheet.^{15,18–20} These calculations, implemented to study the effects of helicity and radius on the electronic structure of SWCNTs, were stimulated by Iijima's observation that many of the individual tubes making up the multiwall tubes he observed were chiral.²⁶ The carbon Slater–Koster parameters characterizing the all-valence tight binding model used in these studies were determined by fits to earlier LDF band-structure calculations on polyacetylene and are given by $V_{ss\sigma} = -4.76$ eV, $V_{sp\sigma} = 4.33$ eV, $V_{pp\sigma} = 4.37$ eV, $V_{pp\pi} = -2.77$ eV, and $\epsilon_p - \epsilon_s = 6$ eV. A comparison of the tight-binding band structure obtained from this all-valence model for the [5,5] tube to the corresponding LDF results is shown in Figure 10.⁴⁵

All-valence tight-binding results for the band gaps of achiral and chiral tubules with a radius up to 1.5 nm are summarized in Figure 11.^{18,20} These results show that no tubules other than the armchair tubules discussed above have a zero band gap at ϵ_F . These results also show that, among those tubules with nonzero band gaps, those with \mathbf{R} such that $n_1 - n_2 = 3q$, with q an integer, have small band gaps as anticipated by Hamada et al.¹⁶ In addition, within this set of small band gap tubules, those with larger chiral angles, Θ , have smaller band gaps than those with similar radii and a smaller value of Θ . Thus, the

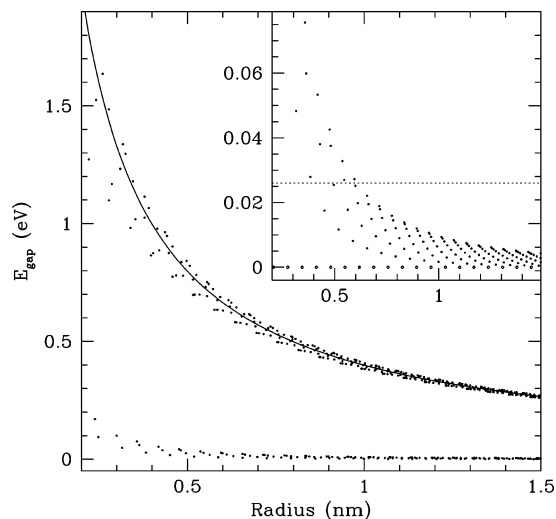


Figure 11. Band gaps predicted by an all-valence tight-binding model for zigzag and chiral tubules (i.e. $[n_1, n_2]$ tubules with $n_1 \neq n_2$) up to 1.5 nm radius. All tubules with $n_1 \neq n_2$ have nonzero band gaps, but tubules with $n_1 - n_2 = 3q$, where q is an integer not equal to zero (solid squares), exhibit much smaller band gaps than tubules with similar radii and with $n_1 - n_2 \neq 3q$ (dots). Data for the small band gap zigzag and chiral tubules ($n_1 - n_2 = 3q$, $q \neq 0$) are presented on an expanded scale in the inset. Also included in the inset are points corresponding to the zero band gap armchair tubules ($n_1 = n_2$). The horizontal dotted line intersecting the inset vertical axis at 0.026 eV corresponds to room temperature. The solid curve in the main portion of the figure is given by $E_{\text{gap}} = |V_{pp\pi}|(d/r)$ and is approximately valid when $n_1 - n_2 \neq 3q$. (Reprinted from ref 18.)

achiral zigzag $\Theta = 0^\circ$ and the armchair $\Theta = 30^\circ$ tubules yield the upper and lower limits for the tubule band gap for a given radius, with the armchair tubules always having zero band gaps.¹⁸ Furthermore, these tight-binding studies imply that all the narrow band gap zigzag and chiral tubules ($n_1 - n_2 = 3q$, $q \neq 0$) have band gaps less than room temperature if their radii exceed ≈ 0.6 nm.¹⁸ Hence, these larger diameter, small band gap zigzag and chiral tubules can be effectively considered to be metals at room temperature. Henceforth, the set of tubes with $n_1 - n_2 = 3q$ will be referred to as “metallic” to indicate that those with $q \neq 0$ have small band gaps. Finally, these and other numerical results show that the band gaps of the large band gap tubes scale approximately as $1/r$,^{18–20} while if the small band gap SWCNTs are grouped into subfamilies with the same Θ , then members of each subfamily have band gaps that scale approximately as $1/r^2$, as shown in Figure 12.³¹

Graphene Sheet Model. Perhaps the simplest model for the electronic structure of SWCNTs is a one-parameter tight-binding model of the graphene sheet with periodic boundary conditions imposed over the rollup vector \mathbf{R} so that

$$\mathbf{k} \cdot \mathbf{R} = 2\pi m \quad (24)$$

where m is an integer.^{14,16,17} This standard one-parameter GSM of SWCNTs, proposed in the earliest theoretical paper on the electronic structure of extended SWCNTs¹⁴ and now supported by many experiments,^{4–13} has been used in successfully predicting many of the fundamental properties of larger diameter carbon nanotubes.^{14–20} These properties include the grouping of SWCNTs as either metallic or semiconducting,^{5,6,14–20} the linear dispersion relations of the metallic tubes in the vicinity of ϵ_F ,^{9,10,14,20} the approximate $1/r$ dependence of the semiconducting band gaps,^{5,6,18–20} the stability of the metallic tubes against a Peierls distortion,^{4,14} and robust ballistic transport through metallic tubes.^{12,13,28} The graphene sheet model has also

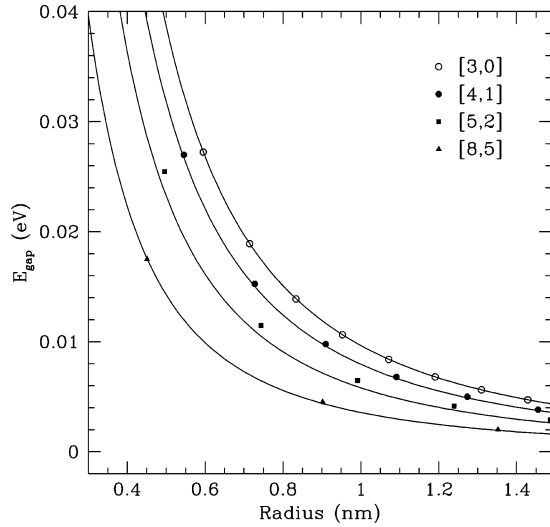


Figure 12. All-valence tight-binding band gaps of several selected families of narrow band gap SWCNTs. The solid lines represent fits to the data using a function of the form A_0/r^2 , which yields a different A_0 for each family. (Reprinted from ref 31.)

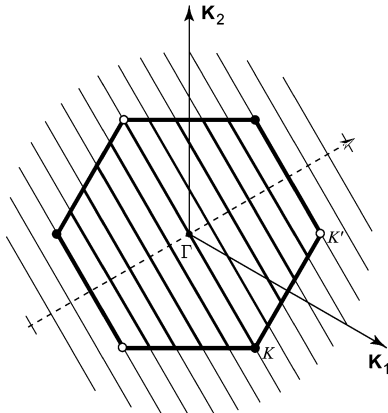


Figure 13. Central Brillouin zone of graphene with the allowed lines for the [5,5] SWCNT depicted. The dashed line is in the direction of \mathbf{R} .

been used to successfully explain and relate the positions of the first few divergent van Hove singularities observed both in metallic and semiconducting SWCNTs in STM experiments.^{36,37}

Graphically, eq 24 restricts the states of graphene allowed for a SWCNT defined by \mathbf{R} to a set of parallel lines in the reciprocal lattice of graphene, with each line corresponding to a different m . Each allowed line is perpendicular to \mathbf{R} and separated from nearest neighboring lines by $2\pi/|\mathbf{R}|$, with the line corresponding to $m = 0$ containing the Γ point at the center of the hexagonal Brillouin zone of graphene.

Within the graphene sheet model, ϵ_F of the tube must remain pinned to its value in graphene. Hence this model will yield metallic armchair SWCNTs, provided the set of states of graphene allowed by eq 24 for these tubes include the K points of Figure 7.¹⁴ That this is true, however, can be seen easily by first recalling that $\mathbf{K}_i \cdot \mathbf{R}_j = 2\pi\delta_{ij}$ and $\mathbf{R} = n\mathbf{R}_1 + n\mathbf{R}_2$ for the armchair SWCNTs and then immediately proving that $(\mathbf{K}_1 - \mathbf{K}_2)/3$ satisfies eq 24 as is demonstrated graphically for the [5,5] tube in Figure 13. Not only does the GSM confirm that armchair nanotubes are metallic, it also provides a fair description of the first-principles π bands of these tubes over the entire 1D zone, especially in the immediate vicinity of ϵ_F where it yields¹⁴ the dispersion relations given by eq 20 or equivalently by eq 21.

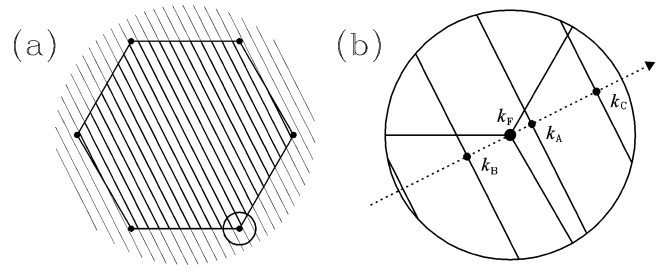


Figure 14. (a) Hexagonal central Brillouin zone of graphene. Parallel lines depict allowed states for [11,9] SWCNT. Circle at bottom right encloses region of states near ϵ_F . (b) Expanded depiction of allowed states near ϵ_F , with dotted line parallel to \mathbf{R} , k_F corner of hexagon with energy ϵ_F , and k_A , k_B , and k_C points of closest approach to k_F on three nearest allowed-state lines in reciprocal space. (Adapted from ref 36.)

The occurrence of the subset of small band gap achiral zigzag and chiral tubules can also be easily understood using the GSM, as can be seen by substituting $\mathbf{R} = n_1\mathbf{R}_1 + n_2\mathbf{R}_2$, and $\mathbf{k}_F = (\mathbf{K}_1 - \mathbf{K}_2)/3$ in eq 24, which immediately shows that these remaining tubes could only be metallic if

$$n_1 - n_2 = 3q \quad (25)$$

where q is an integer with the other tubes semiconductors.^{16,17} However, the GSM implies that the $[n_1, n_2]$ zigzag and chiral tubes satisfying eq 25 are metallic, while the all-valence tight-binding results of Figure 11, as well as earlier results for zigzag tubes,¹⁶ show that they are only narrow band gap semiconductors. This discrepancy arises because of the neglect of curvature effects in the GSM. As with the armchair tubules, curvature slightly shifts the attempted point of crossing away from the K points of graphene. However, in contrast to the corresponding bands for the armchair tubules, these bands have the same symmetry so that they couple, leading to a small gap at ϵ_F .

So long as eq 18 is valid, the one-parameter GSM can be used not only to explain the approximate $1/r$ scaling of the band gaps of the semiconducting tubes seen in Figure 11^{18–20} but also to estimate the positions of the first few peaks nearest the ϵ_F ,³⁶ and ultimately to obtain a universal expression for the DOS valid near the Fermi level that depends only on whether the nanotube is semiconducting or “metallic”.³⁷ More specifically, changing chirality for a given SWCNT radius, r , changes the orientation of lines of allowed states about k_F (located by \mathbf{k}_F) without changing the separation between lines or their distance from k_F . Therefore, semiconducting SWCNTs with similar diameters will have a similar DOS in the vicinity of ϵ_F because $\epsilon_{\pm}(\mathbf{k})$ is radially symmetric about the point k_F .³⁶ Furthermore, because $\epsilon_{-}(\mathbf{k})$ [$\epsilon_{+}(\mathbf{k})$] decreases (increases) with increasing $|\mathbf{k} - \mathbf{k}_F|$, the point of closest approach to k_F in an allowed state line will represent a local maximum (minimum) in the 1D band structure leading to a divergent van Hove singularity in the occupied (unoccupied) DOS.³⁶ The point on the line closest to ϵ_F (labeled as k_A in Figure 14b) also yields the SWCNT band gap. This point is separated from k_F by $|\mathbf{k}_A - \mathbf{k}_F| = 1/(3r)$, one-third the interline spacing^{20,36,37}—a result easily confirmed by projecting $\mathbf{k}_A - \mathbf{k}_F$ along \mathbf{R} . So that k_A generates peaks in the DOS near

$$\epsilon_{\pm}(\mathbf{k}_A) = \epsilon_F \pm E_0 \quad \text{where} \quad E_0 \equiv \frac{|V_{pp\pi}|}{2} \frac{d}{r} \quad (26)$$

and a band gap given by^{18–20}

$$E_{\text{gap}} = \epsilon_{+}(\mathbf{k}_A) - \epsilon_{-}(\mathbf{k}_A) = |V_{pp\pi}| \frac{d}{r} \quad (27)$$

Incrementing by the interline spacing, the next two special points yield peaks in the DOS at $\epsilon_{\pm}(\mathbf{k}_B) = \epsilon_F \pm 2E_0$ and $\epsilon_{\pm}(\mathbf{k}_C) = \epsilon_F \pm 4E_0$.³⁶ This process can then be repeated indefinitely to arrive at a series of peaks located at $\epsilon_F \pm |(3m' + 1)|E_0$, with m' an integer, which should yield good approximations to the peak positions in the DOS of the standard GSM so long as $|(3m' + 1)|d/D \ll 1$, with D the diameter of the nanotube.

A parallel analysis for the “metallic” tubes ($n_1 - n_2 = 3q$) yields a series of peaks located at $\epsilon_F \pm 3|m'|E_0$, with m' a nonzero integer, valid for the standard GSM when $3|m'|d/D \ll 1$.³⁶ This analysis also can be extended to derive a universal expression for the nanotube DOS per carbon atom, $\rho(E)$, that depends only on whether the tube is semiconducting or metallic:³⁷

$$\Lambda|V_{pp\pi}|\rho(E) = \frac{2\sqrt{3}}{\pi^2} \sum_{m'=-\infty}^{\infty} g(E', E_{m'}) \quad (28)$$

where $\Lambda \equiv 2r/d$ and

$$g(E', E_{m'}) = \begin{cases} |E'|/\sqrt{E'^2 - E_{m'}^2} & |E'| > |E_{m'}| \\ 0 & |E'| \leq |E_{m'}| \end{cases} \quad (29)$$

$E' = \Lambda E/|V_{pp\pi}| = E/E_0$, $E_{m'}^2 = (3m' + 1)^2$ for semiconducting ($n_1 - n_2 \neq 3q$), and $E_{m'}^2 = (3m')^2$ for “metallic” ($n_1 - n_2 = 3q$) tubes with q and m' integers, and in writing eq 29 ϵ_F was fixed at zero. In terms of the scaled energy, E' , eq 18 used to derive eq 28 will be a valid approximation to the standard GSM for $|E'| \ll \Lambda$. For SWCNTs with diameters of about 1.4 nm compared to a C–C bond distance in graphene of about 0.14 nm, Λ is about 10 so this translates into a range of energies centered at ϵ_F of about an eV wide. More stringent tests of eq 28 are shown in Figure 15, where comparisons are made between the DOS obtained from eq 28 and those obtained from first-principles LDF calculations.³⁷ These comparisons are for tubes of widely different diameters and helicities and the LDF results were scaled using the appropriate value of Λ and an effective value of $|V_{pp\pi}|$ of 2.5 eV.

The theory described above has many important consequences. First, it predicts that the semiconducting SWCNTs with diameter greater than or approximately equal to C_{60} should have band gaps given approximately by eq 27 when $d/D \ll 1$.^{18–20} This result not only explains the numerical results of Figure 11 but also was used to identify the semiconducting tubes in the initial experiments confirming the existence of these tubes.^{5,6} Second, it shows that semiconducting tubes with about the same diameters should have a similar peak structure near ϵ_F ,³⁶ which explains a puzzle regarding the early data.⁴⁶ Third, for similar diameter semiconducting and “metallic” tubes, it accounts³⁶ for the fact that the observed band gaps of semiconducting tubes are about a factor of 3 smaller than the separation between the first two major peaks nearest ϵ_F in the “metallic” tubes.⁵ Fourth, because Λ is about the same for all semiconducting tubes of similar diameters eq 28 predicts that these tubes will have similar DOS.^{36,37} This has important practical implications because it indicates that if relatively small differences can be tolerated in the electronic structure in the vicinity of ϵ_F , then it is only necessary to sort the semiconducting tubes by their diameters to get the desired properties without concern for their chirality. Similar comments also apply for the “metallic” tubes.^{36,37}

Rather than relying on the linear dispersion relations, approximately valid only so long as $a|\mathbf{k} - \mathbf{k}_F| \ll 1$, the helical and rotational symmetries of SWCNTs can be used to obtain

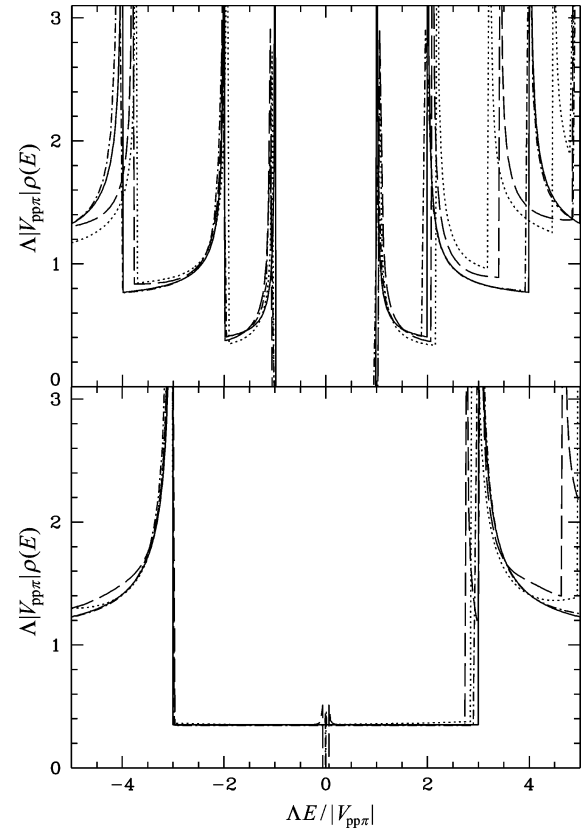


Figure 15. Comparison of scaled first-principles DOS with the universal relationship of eq 28. Top: Solid line depicts results for the universal relationship for semiconducting nanotubes ($n_1 - n_2 \neq 3q$), dotted line depicts scaled first-principles band structure results for [16,0] SWCNT, dashed line depicts results for [13,6] SWCNT, and dot-dashed line depicts results for [21,20] SWCNT. Bottom: Solid line depicts results for the universal relationship for “metallic” nanotubes ($n_1 - n_2 = 3q$), dotted line depicts scaled first-principles band structure results for [10,10] SWCNT, dashed line depicts results for [14,5] SWCNT, and dot-dashed line depicts results for [22,19] SWCNT. (Adapted from ref 37.)

their exact dispersion relations (within the standard GSM) valid over the entire 1D helical zone¹⁹

$$\epsilon_{n\pm}(\kappa) = \epsilon_F \pm |V_{pp\pi}|\sqrt{3 + A_n(\kappa)} \quad (30)$$

where

$$A_n(\kappa) = 2 \cos\left(\frac{n_1\kappa - 2\pi np_1}{N}\right) + 2 \cos\left(\frac{n_2\kappa - 2\pi np_2}{N}\right) + 2 \cos\left(\frac{(n_1 + n_2)\kappa - 2\pi n(p_1 + p_2)}{N}\right) \quad (31)$$

$-\pi \leq \kappa < \pi$, $n = 0, \dots, N - 1$, p_1 and p_2 are given by eq 9, and N is the largest common divisor of n_1 and n_2 . If n_1 and n_2 are relatively prime, then $N = 1$ so that eq 30 reduces to

$$\epsilon_{0\pm}(\kappa) = \epsilon_F \pm$$

$$|V_{pp\pi}|\sqrt{3 + 2 \cos n_1\kappa + 2 \cos n_2\kappa + 2 \cos (n_1 + n_2)\kappa} \quad (32)$$

Thus, as a consequence of screw symmetry, a SWCNT such as the [10,9] has only a single bonding and a single antibonding band within the standard GSM. This is in marked contrast to the 1084 bands that would be drawn if a zone folding method were used to obtain the [10,9] band structure. Note that eq 30 can be directly obtained from eq 17 by first using eqs 1, 8, and

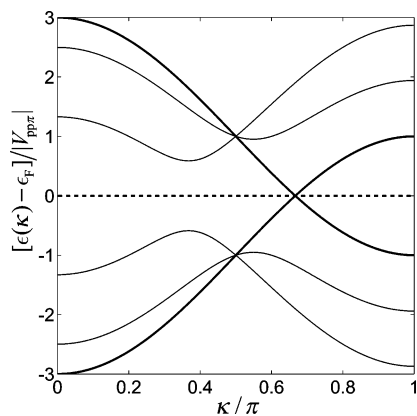


Figure 16. Band structures of [5,5] SWCNT from the standard GSM as a function of the helical phase factor κ from 0 to π obtained by assuming that $\phi = \pi$. The invariant bands that cross at ϵ_F are depicted as heavy black lines. The bands at $-\kappa$ are the same as those at κ . Hence, results are plotted over only half of the central 1D zone.

9 to show that $\mathbf{R}_1 = (p_2\mathbf{R} - n_2\mathbf{H})/N$ and $\mathbf{R}_1 = (n_1\mathbf{H} - p_1\mathbf{R})/N$, and then using these expressions in eq 17, while recalling eqs 15 and 24.

Results for the band structure for the [5,5] SWCNT obtained from eq 30 are shown in Figure 16. These results can be directly compared to the corresponding all-valence and LDF results of Figure 10. It is also worthwhile to compare Figure 16 to Figure 9a. Though apparently different, both depict band structures for the [5,5] tube obtained from eq 30. The differences arise because a twist angle of $\phi = \pi/5$ ($p_2 = 1, p_1 = 0$) was assumed in obtaining Figure 9a, while $\phi = \pi$ ($p_2 = 3, p_1 = 2$) was assumed in obtaining Figure 16. Either equally valid choice is allowed by eq 9 for the [5,5] SWCNT and will yield identical results for any measurable property. Fewer distinct bands are visible in Figure 16 because $\phi = \pi$ yields bands that are also eigenstates of the symmetry operations of the full C_{5v} point group, which includes the doubly degenerate e_1 and e_2 representations.

It is important to understand not only the successes but also the limitations of the GSM. To begin, eq 18, and the results that follow from it, are valid as an approximation to the one-parameter GSM only so long as $a|\mathbf{k} - \mathbf{k}_F| \ll 1$. Thus, the approximate expression for E_{gap} will worsen for smaller and smaller diameter tubes as the separation between allowed state lines increases.^{36,37} Also, estimates of the peak locations for a given tube will worsen for peaks more and more distant from ϵ_F .^{36,37} This breakdown of the radial approximation (termed trigonal warping⁴⁷ to reflect the 3-fold symmetry that $\epsilon(\mathbf{k})$ must ultimately exhibit about the K points of graphene) will be reflected in the precise peak locations^{37,47,48} and has been exploited in sufficiently resolved experiments to distinguish two semiconducting tubes of similar diameters but different chiralities. The same can also be said for the “metallic” tubes where, for example, splitting of the first major peak will differentiate a metallic armchair tube from a chiral or zigzag “metallic” tube of similar diameter.³⁷ Note, however, that even if trigonal warping is treated exactly within the standard GSM by using eq 30, this model itself is only an approximation to more sophisticated one-electron calculations even at the graphene sheet level. Thus, if LDF results for the graphene sheet were used to construct the peak locations by applying eq 24 to those first-principles results, then peak locations somewhat different than those obtained from the one-parameter GSM model would be found, even if trigonal warping effects are included exactly. This is because the LDF band structure, for tubes with diameters of typical experimental interest, show a breakdown in particle

hole symmetry around ϵ_F , which initially is small but increases as the energy recedes from ϵ_F .^{14,20,37} Although such a loss of particle hole symmetry in the standard GSM can be included by introducing an additional parameter arising from overlap,³⁹ there are other one-electron effects that can be of equal or greater importance that still should be accounted for. Principal among these is the interaction between π and σ orbitals (hybridization effects), which exist in the tube but not in the GSM at whatever level it is implemented. It is these interactions that play a dominant role in converting the chiral and zigzag tubes predicted to be metals in the GSM to small band gap semiconductors. Also, a comparison between the results for the semiconducting band gaps for tubes with $n_1 - n_2 \neq 3q$ at both the all-valence^{18,20} and one-parameter GSM level¹⁹ shows that hybridization effects can be more important than trigonal warping. Thus, great care must be taken before ascribing deviations from the one-parameter GSM predictions to one effect or another, even at the one-electron level.

It might be supposed that the failure of the GSM to predict small band gap semiconductors rather than metals can be corrected by taking into account that the nearest neighboring C–C π matrix elements are no longer all equal when the sheet is rolled up into a tube. However, within the all-valence tight-binding model, the band gaps of these small tubes is given to lowest order in d/r by

$$\tilde{E}_{\text{gap}} = \frac{3}{4} \left(\frac{V_{pp\pi} + V_{pp\sigma}}{V_{pp\pi} - V_{pp\sigma}} \right) V_{pp\pi} \left(\frac{d}{r} \right)^2 |\cos 3\Theta| \quad (33)$$

a result which can only be obtained by including interactions with σ states some 10 eV distant from ϵ_F .⁴⁹

Finally, attention so far has been restricted to SWCNTs with diameters equal to or somewhat greater than $(I_h) C_{60}$. Nevertheless, smaller diameter nanotubes have been observed either as the central shell of a multiwall carbon nanotube,⁵⁰ encased in the channels of a porous zeolite crystal,⁵¹ or perpendicularly anchored to larger nanotubes.⁵² Furthermore, consistent with earlier semiempirical results,^{53,54} total energy LDF calculations have shown that SWCNTs with diameters as small as 0.38 nm, if isolated, would be stable against unzipping along the nanotube axis.⁵⁵ The LDF calculations predict that these narrow SWCNTs can be either semiconductors or metals but often do not have an electronic structure that can be understood based on the GSM.^{55–57} Also, for these narrow SWCNTs, many-body effects should prove increasingly important.⁵⁵

Comparisons to Experiment

The remarkable combination of properties predicted for armchair SWCNTs¹⁴ helped stimulate worldwide efforts first to synthesize these tubes^{22–24} and then measure their properties, with the first STM results confirming directly that these tubes were metallic to far below room temperature reported in 1997.⁴ In 1998 it was subsequently found that the other tubes were indeed either “metallic” (the experiments were not sufficiently resolved to differentiate the truly metallic tubes from small band gap semiconductors) or semiconducting,^{5,6} as anticipated by theory,^{14–18} with the semiconducting tubes exhibiting band gaps that scaled as predicted by eq 27 with an experimentally measured value of $|V_{pp\pi}|$ close to that obtained from the first-principles calculations.²⁰ Next, ¹³C nuclear magnetic resonance studies⁸ showed that metallic SWCNTs had a DOS at ϵ_F that scaled as predicted by eq 23 with a measured value of $\rho(E)$ consistent with the theoretical value. Later, experiments were reported that showed directly that the dispersion relations of

the metallic and small band gap tubes were indeed just as anticipated by theory,^{14,20} with an experimentally measured value of the Fermi velocity^{9,10} close to that implied by the first-principles results.²⁰ Also, highly resolved STM results were reported¹¹ that showed not only that armchair nanotubes were truly metallic¹⁴ but also that the small band gap tubes have gaps that scale as predicted by theory^{31,32} with a coefficient very close to that found from the all-valence tight-binding calculations.¹⁸

These pioneering experimental studies also stimulated new theoretical work and then new experiments. Thus, the 1997 experiments⁴ confirming that the armchair nanotubes were metallic and stable against a spontaneous symmetry breaking¹⁴ also showed directly that these tubes could maintain ballistic transport over at least 140 nm in the presence of residual disorder. Furthermore, these experiments suggested that the nanotube wave functions extended over the entire 3 μm length of the tube.⁴ This in turn led to theoretical studies that concluded that these tubes should be exceptional ballistic conductors,^{28,29} as was later directly observed.^{12,13} Also, the 1998 experiments^{5,6} confirming that SWCNTs were either semiconducting or “metallic”^{14–18} with semiconducting band gaps that scaled as $1/r$ (refs 18–21) raised new questions⁴⁶ which in turn led to extensions³⁶ of the initial band gap analysis^{19,20} to ultimately arrive at the universal expression for the nanotube DOS near ϵ_F ;³⁷ these theoretical results were then used in interpreting later experimental STM data.^{34,35} Finally, the 2001 experiments¹¹ showing that the band gaps of the small band gap nanotubes indeed scaled as $1/r^2$ ^{31,32} stimulated the analysis that led to an analytic expression for the scaling coefficient in terms of the all-valence model parameters.⁴⁹ These are but a few examples of the strong interplay between theory and experiment that the field of SWCNTs has enjoyed.

Some Current Opportunities

The present level of agreement between the fundamental one-electron theory of SWCNTs discussed in this article and STM experiments on tubes with diameters greater than or equal to I_h C_{60} is good. There remain, however, many opportunities for further study even at a fundamental level.

Consider, for example, recent spectrofluorimetric measurements on SWCNTs isolated in aqueous surfactant suspensions which have been used to assign the structure of more than 30 different semiconducting tubes.^{58,59} These assignments rely heavily on correlating systematic deviations from the universal DOS obtained from a tight-binding model with corresponding deviations identified in the experimental data. These deviations turn out to have a relatively small but distinct chirality dependence. Once the assignments are made, the transition energies between the first couple of van Hove singularities can be graphed as a function of diameter.⁵⁹ (Owing to the helical symmetry of these tubes, electric dipole transitions must either be vertical $\kappa = \kappa'$ or differ by the helical twist angle $\kappa' = \kappa \pm \phi$, and hence transitions such as $\nu_2 \rightarrow c_1$ or $c_2 \rightarrow \nu_1$ are not dipole allowed for polarizations parallel to the nanotube axis, but can be allowed by polarizations transverse to the nanotube axis.⁶⁰) In agreement with predictions^{36,37} these graphs show that semiconducting tubes with similar diameters have similar transition energies (E_{11} and E_{22}) on the scale of E_{11} and E_{22} without regard to their chirality. Also as anticipated by theory,^{36,37} the experimental results show that the standard deviation of these transition energies for tubes of similar diameter increases for smaller diameter tubes, and for a group of tubes of similar diameter the standard deviation in E_{22} is greater than E_{11} . In addition, the graphs show patterns in for

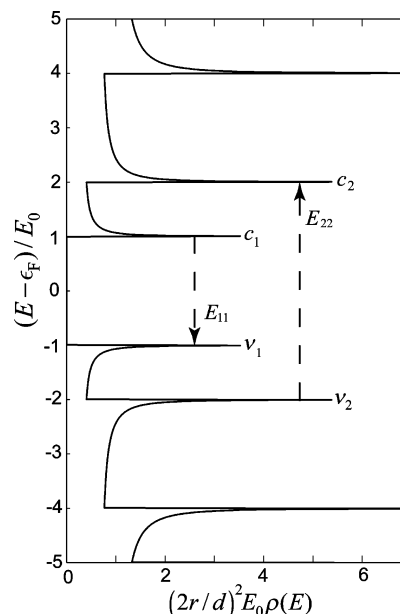


Figure 17. Universal DOS for semiconducting SWCNTs with the transitions identified in ref 58 depicted.

example E_{11} that were found in theoretical calculations obtained prior to even the successful synthesis of SWCNTs.¹⁸ However, these experimental assignments have raised new questions. Specifically, consistent with STM results, the ratio E_{22}/E_{11} will be to a good approximation a constant given by $4E_0/2E_0 = 2$ so long as $2d/D \ll 1$, where d is the C–C bond distance and D the nanotube diameter.^{36,37} However, the data, although not well into the regime $2d/D \ll 1$, suggests that this ratio is tending to 1.8 not 2. This 10% discrepancy has been attributed to many-body effects present in the optical data but absent from the STM data, which is plausible.⁶¹ More interesting, however, is the fact that the magnitude of $V_{pp\pi}$ estimated from the optical data for E_{11} turns out to be on the order of an eV larger than the corresponding quantity estimated from STM data. Explanations have begun to emerge but the situation is far from settled.⁶² Assuming that the assignments are correct, any successful resolution must simultaneously account for the STM data (largely explained by the effective one-electron theory described above) and the optical data and hence will likely involve many-body effects present in the optical but not the STM data. An obvious candidate is electron–hole pair interactions leading to exciton formation.⁶³ However, even at the LDF level no comprehensive calculations have been made to confirm that the patterns associated with chirality found in the tight-binding calculations persist at this higher level of approximation. Another issue involves the relative transition probabilities for allowed optical transitions. For example, transitions such as $\nu_2 \rightarrow c_1$ or $c_2 \rightarrow \nu_1$ should be symmetry-allowed for light polarization transverse to the nanotube axes, but some theoretical studies have suggested that depolarization effects could suppress their intensities.^{64,65} Furthermore, no zigzag SWCNTs are found based on a tight-binding model motivated interpretation of the spectrofluorimetric data.⁵⁸ However, confirmation of their absence will require a better understanding of the selection rules and optical transition probabilities in SWCNTs.

Another opportunity is to identify and better understand the dominant scattering processes limiting nanotube transport with an eye toward tailoring the tube and its environment either to enhance or diminish their effects. Such an improved understanding could lead to counterintuitive conclusions with important technological implications. For example, it might seem that an

isolated metallic tube at finite temperature would exhibit ballistic transport over a larger distance than the same tube lying on a substrate, but this need not be the case. In particular, long wavelength twistons are thought to provide an important contribution to the resistance of isolated nanotubes at finite temperatures.⁶⁶ However, due to pinning, such excitations might be effectively quenched by laying the tube on a substrate.²⁸ Of course there is a price to be paid in the tube–substrate interactions which will introduce new scattering processes. However, the characteristic mean free path for elastic electron backscattering associated with such substrate interactions is expected to be very long²⁸ and hence might not be dominant in determining the distance over which the tube can maintain ballistic transport. Thus, if conditions are right, a metallic tube might be a better ballistic conductor if it is lying on a substrate rather than suspended above it. In a related vein, the length of the tube rather than its environment can be adjusted to alter its behavior. Any scattering process in the tube (either elastic or inelastic) will have a characteristic length associated with it that can be estimated from its scattering rate given by Fermi's golden rule and the Fermi velocity. With carbon nanotubes one has the opportunity to alter their lengths with the intent of either diminishing or enhancing these effects. For example, if one wants to use a carbon nanotube as a sensor, then it would probably be best to work at a length shorter than but not too far from where all the states would be expected to become localized due to residual disorder. At this length transport through the tube is expected to be more sensitive to perturbations introduced by foreign chemical species interacting with the surface of the tube.³⁰ On the other hand, if one wants to work in a ballistic regime, then simply shortening the tube to the point that its length is shorter than the shortest characteristic length associated with the scattering process, which ruins ballistic transport for the conditions of the experiment, is obviously the way to go.⁶⁷

Concluding Remarks

The field of nanotubes continues to advance rapidly. Already transistors^{68–70} and logic circuits^{71,72} have been constructed from SWCNTs, and these tubes have been identified as leading candidates to replace silicon in some 21st century electronic devices,⁷³ establishing SWCNTs as an important early example of materials by design. Perhaps SWCNTs will be components of future computers used to design new materials with even more remarkable properties.

Acknowledgment. This work was supported by the Office of Naval Research, both directly and through the Naval Research Laboratory. D. H. Robertson is thanked for help with several of the figures.

References and Notes

- (1) Kroto, H. W.; Heath, J. R.; O'Brien, S. C.; Curl, R. F.; Smalley, R. E. *Nature* (London) **1985**, *318*(6042), 162–163.
- (2) Tibbetts, G. G. *J. Cryst. Growth* **1984**, *66*(3), 632–638.
- (3) Shirakawa, H.; Louis, E. J.; MacDiarmid, A. G.; Chiang, C. K.; Heeger, A. J. *J. Chem. Soc., Chem. Commun.* **1977**, *16*, 578–580.
- (4) Tans, S. J.; Devoret, M. H.; Dai, H. J.; Thess, J.; Smalley, R. E.; Geerligs, L. J.; Dekker, C. *Nature* (London) **1997**, *386*(6624), 474–477.
- (5) Wildöer, J. W. G.; Venema, L. C.; Rinzler, A. G.; Smalley, R. E.; Dekker, C. *Nature* (London) **1998**, *391*(6662), 59–62.
- (6) Odom, T. W.; Huang, J.-L.; Kim, P.; Lieber, C. M. *Nature* (London) **1998**, *391*(6662), 62–64.
- (7) Venema, L. C.; Wildöer, J. W. G.; Janssen, J. W.; Tans, S. J.; Tuinstra, H. L. J. T.; Kouwenhoven, L. P.; Dekker, C. *Science* **1999**, *283*(5398), 52–55.
- (8) Tang, X.-P.; Kleinhammes, A.; Shimoda, H.; Fleming, L.; Benounne, K. Y.; Sinha, S.; Bower, C.; Zhou, O.; Wu, Y. *Science* **2000**, *288*(5465), 492–494.
- (9) Lemay, S. G.; Janssen, J. W.; van den Hout, M.; Mooij, M.; Bronikowski, M. J.; Willis, P. A.; Smalley, R. E.; Kouwenhoven, L. P.; Dekker, C. *Nature* (London) **2001**, *412*(6847), 617–620.
- (10) Ouyang, M.; Huang, J.-L.; Lieber, C. M. *Phys. Rev. Lett.* **2002**, *88*(6), 066804-1–066804-4.
- (11) Ouyang, M.; Huang, J.-L.; Cheung, C. L.; Lieber, C. M. *Science* **2001**, *292*(5517), 702–705.
- (12) Liang, W. J.; Bockrath, M.; Bozovic, D.; Hafner, J. H.; Tinkham, M.; Park, H. *Nature* **2001**, *411*(6838), 665–669.
- (13) McEuen, P. L.; Bockrath, M.; Cobden, D. H.; Yoon, Y.-G.; Louie, S. G. *Phys. Rev. Lett.* **1999**, *84*(24), 5098–5101.
- (14) Mintmire, J. W.; Dunlap, B. I.; White, C. T. *Phys. Rev. Lett.* **1992**, *68*(5), 631–634.
- (15) Mintmire, J. W.; Robertson, D. H.; Dunlap, B. I.; Mowrey, R. C.; Brenner, D. W.; White, C. T. In *Electrical, Optical, and Magnetic Properties of Organic Solid State Materials*; Chiang, L. Y., Garito, A. F., Sandman, D. J., Eds.; MRS Symposia Proceedings; Materials Research Society: Pittsburgh, 1992; Vol. 247, pp 339–342.
- (16) Hamada, N.; Sawada, S.; Oshiyama, A. *Phys. Rev. Lett.* **1992**, *68*(10), 1579–1581.
- (17) Saito, R.; Fujita, M.; Dresselhaus, G.; Dresselhaus, M. S. *Appl. Phys. Lett.* **1992**, *60*(18), 2204–2206.
- (18) White, C. T.; Mintmire, J. W.; Mowrey, R. C.; Brenner, D. W.; Robertson, D. H.; Harrison, J. A.; Dunlap, B. I. In *Buckminsterfullerenes*; Billups, W. E.; Ciufolini, M. A., Eds.; VCH Publishers: New York, 1993; pp 125–184.
- (19) White, C. T.; Robertson, D. H.; Mintmire, J. W. *Phys. Rev. B* **1993**, *47*(9), 5485–5488.
- (20) Mintmire, J. W.; Robertson, D. H.; White, C. T. *J. Phys. Chem. Solids* **1993**, *54*(12), 1835–1840.
- (21) Ajiki, H.; Ando, T. *J. Phys. Soc. Jpn.* **1993**, *62*(4), 1255–1266.
- (22) Iijima, S.; Ichihashi, T. *Nature* (London) **1993**, *363*(6430), 603–605.
- (23) Bethune, D. S.; Kiang, C. H.; Devries, M. S.; Gorman, G.; Savoy, R.; Vazquez, J.; Beyers, R. *Nature* (London) **1993**, *363*(6430), 605–607.
- (24) Thess, A.; Lee, R.; Nikolaev, P.; Dai, H. J.; Petit, P.; Robert, J.; Xu, C. H.; Lee, Y. H.; Kim, S. G.; Rinzler, A. G.; Colbert, D. T.; Scuseria, G. E.; Tomanek, D.; Fischer, J. E.; Smalley, R. E. *Science* **1996**, *273*(5274), 483–487.
- (25) Ebbesen, T. W.; Ajayan, P. M. *Nature* (London) **1992**, *358*(6383), 220–222.
- (26) Iijima, S. *Nature* (London) **1991**, *354*(6348), 56–58.
- (27) Krätschmer, W.; Lamb, L. D.; Fostiropoulos, K.; Huffman, D. R. *Nature* (London) **1990**, *347*(6291), 354–358.
- (28) White, C. T.; Todorov, T. N. *Nature* (London) **1998**, *393*(6682), 240–242.
- (29) Ando, T.; Nakanishi, T. *J. Phys. Soc. Jpn.* **1998**, *67*(5), 1704–1713.
- (30) White, C. T.; Todorov, T. N. *Nature* (London) **2001**, *411*(6838), 649–651.
- (31) White, C. T.; Robertson, D. H.; Mintmire, J. W. In *Clusters and Nanostructured Materials*; Jena, P., Behara, S. N., Eds.; Nova Science Publishers: New York, 1996; pp 231–237.
- (32) Kane, C. L.; Mele, E. J. *Phys. Rev. Lett.* **1997**, *78*(10), 1932–1935.
- (33) Ando, T. *Solid State Commun.* **2003**, *127*(2), 69–78 and references therein.
- (34) Venema, L. C.; Janssen, J. W.; Buitelaar, M. R.; Wildöer, J. W. G.; Lemay, S. G.; Kouwenhoven, L. P.; Dekker, C. *Phys. Rev. B* **2000**, *62*(8), 5238–5244.
- (35) Kim, P.; Odom, T. W.; Huang, J.-L.; Lieber, C. M. *Phys. Rev. Lett.* **1999**, *82*(6), 1225–1228.
- (36) White, C. T.; Mintmire, J. W. *Nature* (London) **1998**, *394*(6688), 29–30.
- (37) Mintmire, J. W.; White, C. T. *Phys. Rev. Lett.* **1998**, *81*(12), 2506–2509.
- (38) Robertson, D. H.; Brenner, D. W.; Mintmire, J. W. *Phys. Rev. B* **1992**, *45*(21), 12592–12595.
- (39) Wallace, P. R. *Phys. Rev.* **1947**, *71*(9), 622–634.
- (40) Painter, G. S.; Ellis, D. E. *Phys. Rev. B* **1970**, *1*(12), 4747–4752.
- (41) Mintmire, J. W.; White, C. T. *Phys. Rev. Lett.* **1983**, *50*(2), 101–105.
- (42) Mintmire, J. W. In *Density Functional Methods in Chemistry*; Labanowski, J. K., Andzelm, J. W., Eds.; Springer-Verlag: New York, 1991; pp 125–137.
- (43) Peierls, R. E. *Quantum Theory of Solids*; Oxford University Press: New York, 1955.

- (44) Frank, S.; Poncharal, P.; Wang, Z. L.; de Heer, W. A. *Science* **1998**, 280(5370), 1744–1746.
- (45) Mintmire, J. W.; White, C. T. In *Carbon Nanotubes: Preparation and Properties*; Ebbesen, T. W., Ed.; CRC Press: New York, 1997; pp 191–224.
- (46) Dresselhaus, M. S. *Nature* (London) **1998**, 391(6662), 19–20.
- (47) Saito, R.; Dresselhaus, G.; Dresselhaus, M. S. *Phys. Rev. B* **2000**, 61(4), 2981–2990.
- (48) Reich, S.; Thomsen, C. *Phys. Rev. B* **2000**, 62(7), 4273–4276.
- (49) White, C. T.; Cabria, I.; Mintmire, J. W., unpublished.
- (50) Qin, L.-C.; Zhao, X.; Hirahara, K.; Miyamoto, Y.; Ando, Y.; Iijima, S. *Nature* (London) **2000**, 408(6808), 50.
- (51) Wang, N.; Tang, Z. K.; Li, G. D.; Chen, J. S. *Nature* (London) **2000**, 408(6808), 50–51.
- (52) Peng, L.-M.; Zhang, Z. L.; Xue, Z. Q.; Wu, Q. D.; Gu, Z. N.; Pettifor, D. G. *Phys. Rev. Lett.* **2000**, 85(15), 3249–3252.
- (53) Sawada, S.; Hamada, N. *Solid State Commun.* **1992**, 83(11), 917–919.
- (54) Lucas, A. A.; Lambin, P. H.; Smalley, R. E. *J. Phys. Chem. Solids* **1993**, 54(5), 587–593.
- (55) Cabria, I.; Mintmire, J. W.; White, C. T. *Phys. Rev. B* **2003**, 67(12), 121406-1–121406-4.
- (56) Machón, M.; Reich, S.; Thomsen, C.; Sanchez-Portal, D.; Ordejon P. *Phys. Rev. B* **2002**, 66(15), 155410-1–155410-5.
- (57) Blase, X.; Benedict, L. X.; Shirley, E. L.; Louie, S. G. *Phys. Rev. Lett.* **1994**, 72(12), 1878–1881.
- (58) Bachilo, S. M.; Strano, M. S.; Kittrell, C.; Hauge, R. H.; Smalley, R. E.; Weisman, R. B. *Science* **2002**, 298(5602), 2361–2366.
- (59) Weisman, R. B.; Bachilo, S. M.; Tsybolski, D. *Appl. Phys. A* **2004**, 78(8), 1111–1116.
- (60) Mintmire, J. W.; White, C. T. *Synth. Met.* **1996**, 77 (1–3), 231–234.
- (61) Kane, C. L.; Mele, E. J. *Phys. Rev. Lett.* **2003**, 90(20), 207401-1–207401-4.
- (62) Hideaki, S.; Suzuura, H.; Ando, T. *J. Phys. Soc. Jpn.* **2003**, 72(7), 1698–1705.
- (63) Ando, T. *J. Phys. Soc. Jpn.* **1997**, 66(4), 1066–1073.
- (64) Ajiki, H.; Ando T. *Physica B* **1994** 201, 349–352.
- (65) Marinopoulos, A. G.; Reining, L.; Rubio, A.; Vast, N. *Phys. Rev. Lett.* **2003**, 91 (4), 046402-1–046402-4.
- (66) Kane, C. L.; Mele, E. J.; Lee, R. S.; Fischer, J. E.; Petit, P.; Dai, H.; Thess, A.; Smalley, R. E.; Verschuere, A. R. M.; Tans, S. J.; Dekker, C. *Europhys. Lett.* **1998**, 41(6), 683–688.
- (67) Javey, A.; Guo, J.; Paulsson, M.; Wang, Q.; Mann, D.; Lundstrom, M.; Dai, H. *Phys. Rev. Lett.* **2004**, 92(10), 106804-1–106804-4.
- (68) Tans, S. J.; Verschuere, A. R. M.; Dekker, C. *Nature* (London) **1998**, 393(6680), 49–52.
- (69) Martel, R.; Schmidt, T.; Shea, H. R.; Hertel, T.; Avouris, Ph. *Appl. Phys. Lett.* **1998**, 73(17), 2447–2449.
- (70) Postma, H. W. C.; Teepen, T.; Yao, Z.; Grifoni, M.; Dekker, C. *Science* **2001**, 293(5527), 76–79.
- (71) Bachtold, A.; Hadley, P.; Nakanishi, T.; Dekker, C. *Science* **2001**, 294(5545), 1317–1320.
- (72) Derycke, V.; Martel, R.; Appenzeller, J.; Avouris, Ph. *Nano Lett.* **2001**, 1(9), 453–456.
- (73) Jacoby, M. *Chem. Eng. News* **2002**, 80(22), 9.